OPEN ACCESS

Haya: The Saudi Journal of Life Sciences
Abbreviated Key Title: Haya Saudi J Life Sci
ISSN 2415-623X (Print) | ISSN 2415-6221 (Online)
Scholars Middle East Publishers, Dubai, United Arab Emirates
Journal homepage: https://saudijournals.com

Original Research Article

Single-Atom Engineered Nanorings for Efficient Nitrogen Reduction: A DFT Study

Sana Ullah[1], Sameer Khan[2], Wasif Ullah[3], Mehboob Khan[1]*, Sadiq Ur Rehman[4], Zafar Ullah[4], Waqas Khan[1]

[1]Department of Chemistry, Hazara University, Mansehra, Pakistan
[2]Department of Chemistry, Comsats University Islamabad, Abbottabad Campus
[3]Department of Chemistry, Government Post Graduate College Lakki Marwat, Pakistan
[4]Department of Chemistry, Kohat University of Science and Technology

DOI: https://doi.org/10.36348/sjls.2025.v10i11.003 | **Received:** 14.10.2025 | **Accepted:** 05.12.2025 | **Published:** 09.12.2025

***Corresponding author:** Mehboob Khan
Department of Chemistry, Hazara University, Mansehra, Pakistan

Abstract

This work presents a comprehensive density functional theory (DFT) investigation of the nitrogen reduction reaction (NRR) on transition-metal (TM) atoms (Cr, Ni, Ru, Rh) supported on double nanorings (NRs = B_8N_8, B_8P_8, Al_8N_8, Al_8P_8, Ga_8N_8) via the distal pathway. The study focuses on elucidating the energetics, stability, and electronic properties of these TM-decorated nanorings as potential electrocatalysts for efficient nitrogen fixation. Geometry optimizations were performed using the long-range-corrected, range-separated functional ωB97XD combined with the polarized triple-ζ def2-TZVP basis set augmented with diffuse s and p functions. Interaction energies reveal that Ru@B_8N_8 is the most stable configuration, exhibiting a strong binding energy of −5.78 eV. Owing to this high stability, Ru@B_8N_8 was selected for detailed mechanistic evaluation of electrochemical NRR. A mixed-basics approach was employed in which Ru was treated using the LANL2DZ effective core potential, while B, N, and H atoms were described with the 6-31G(d,p) basis set to balance computational efficiency and accuracy. Charge-transfer interactions were analyzed using natural bond orbital (NBO) methods, and further insight into the electronic structure was obtained through frontier molecular orbital (FMO) and density of states (DOS) analyses, including evaluation of HOMO–LUMO energy gaps. Overall, this work provides fundamental insights into the stability and catalytic behavior of TM-supported double nanorings and offers valuable guidance for the rational design of robust and highly active NRR electrocatalysts.

Keywords: Density Functional Theory, Nitrogen Reduction Reaction, Transition Metal, Frontier Molecular Orbitals, Density of States, Natural Bond Orbital.

1. INTRODUCTION

Ammonia plays a critical role across multiple sectors, including chemical fertilizer production, industrial synthesis, and energy storage applications [1]. It is also the major reduced nitrogen species in the atmosphere, with agricultural activities serving as its primary emission source [2]. As an alkaline atmospheric gas, ammonia (NH_3) significantly contributes to haze formation and environmental degradation. Synthetic ammonia, produced predominantly through the Haber–Bosch process, remains indispensable to global agriculture as the primary nitrogen source for fertilizers. The introduction of ammonia-based fertilizers such as urea and ammonium nitrate transformed global food production, enabling large-scale, high-yield agriculture. Nearly half of the world's population depends on nitrogen fertilizers for food security, and without synthetic ammonia, worldwide agricultural output would decline sharply, resulting in food shortages and increased malnutrition [3]. Nitrogen-based fertilizers are essential for maximizing crop yields because nitrogen is the most limiting nutrient in plant growth. Most widely used fertilizers including urea, ammonium nitrate, and ammonium sulfate are synthesized from ammonia and nitric acid. Consequently, global demand for ammonia closely follows population growth and changing dietary patterns, which influence agricultural intensity and fertilizer consumption [4]. Beyond agriculture, ammonia is an important industrial chemical and is increasingly recognized as a promising carbon-free energy carrier. Its potential as a clean fuel, an energy storage medium, and a transport vector for renewable energy has generated significant interest. Plasma-enabled ammonia synthesis offers a sustainable alternative to fossil-fuel-derived

production routes and can help lower carbon emissions while increasing flexibility in decentralized energy systems [5]. The well-established infrastructure for ammonia storage and transportation also supports its emerging role in renewable energy systems. Recent research efforts focus on both historical developments and modern innovations to position ammonia as a next-generation sustainable energy carrier [6]. The environmental impact of ammonia production depends heavily on the energy source. Life-cycle assessments reveal that coal-based routes generate the highest greenhouse gas emissions, with values reaching 13.6 kg CO_2 kg^{-1} NH_3. In contrast, nuclear-powered electrolysis can reduce emissions to as low as 0.48 kg CO_2 kg^{-1} NH_3, underscoring the importance of cleaner energy inputs for sustainable ammonia synthesis [7]. Historically, ammonia has supported approximately 27 % of the world's population through fertilizer applications [8]. The Haber Bosch process, developed by Fritz Haber in 1908 and industrialized by Carl Bosch in 1911, enabled large-scale NH_3 synthesis from N_2 and H_2 under high temperature and pressure [9]. This process remains energy-intensive because breaking the N≡N triple bond requires substantial input energy, largely sourced from fossil fuels leading to 1–2 % of global CO_2 emissions [10, 11]. Thus, the development of low-carbon or carbon-neutral NH_3 synthesis technologies is crucial for meeting climate-mitigation goals. Biological nitrogen fixation (BNF), facilitated by symbiotic and free-living nitrogen-fixing microbes, provides a natural alternative for converting N_2 into bioavailable nitrogen [12, 13]. However, the efficiency of BNF is limited by environmental factors, plant–microbe interactions, and competition with synthetic fertilizer inputs [14]. Nitrogenase enzymes including Mo-, V-, and Fe-only nitrogenases play central roles in BNF, with Mo-nitrogenase believed to have originated in methanogenic archaea [15]. Electrochemical nitrogen reduction reaction (E-NRR) has gained momentum as a green alternative to the Haber–Bosch process because it uses water and nitrogen as feedstocks under ambient conditions. However, low ammonia yields, poor Faradaic efficiency, and interference from contaminants remain significant barriers [16]. To improve catalytic performance, researchers have explored the design of catalysts with enhanced active-site exposure and tailored electronic structures. Recent advances span noble-metal, non-noble-metal, single-atom, and metal-free electrocatalysts, with theory experiment integration providing mechanistic insight and guiding rational catalyst design [17, 18]. Accurate modeling of electrode potential and pH is also essential, as shown by studies on graphyne-confined Mo single-atom catalysts (Mo-TEB), where improved NRR activity correlates with d-band center proximity to the Fermi level and enhanced magnetic moments [19–21]. Inspiration from the FeMo-cofactor (FeMoco) of nitrogenase has further advanced understanding of N_2 activation. Iron(I) and iron (0) complexes have shown the ability to weaken or break the N≡N bond at low temperatures, facilitated by multi-metal cooperation and alkali-metal interactions [22]. Moreover, NRR efficiency is strongly limited by competition with the hydrogen evolution reaction (HER); nitrogen adsorption and hydrogenation steps are highly sensitive to electrode potential and N_2 availability, making N_2 transportation and concentration at the interface critical [23]. Single-atom catalysts (SACs) have attracted considerable interest due to their maximum atom efficiency, uniform coordination environments, and tunable electronic properties. SACs supported on nanostructures—including carbon cages, BN cages, and metal–organic frameworks have demonstrated strong potential for N_2 activation under ambient conditions [24–26]. Computational screening, especially DFT-based analysis, has accelerated the discovery of promising SAC systems by predicting adsorption energies, stability, and potential-determining steps across a wide range of transition metals and nanocage supports [27, 28]. Transition-metal centers (e.g., Fe, Mo, Co, Ru, V) play decisive roles in catalytic performance through their d-orbital occupancy, oxidation states, and binding affinities to N_2 and reaction intermediates [29–31]. Selectivity against HER is particularly influenced by hydrogen vs nitrogen adsorption energies, emphasizing the importance of appropriate metal choice and support interactions [32]. Strong metal–support interactions (SMSI) stabilize isolated metal atoms, prevent aggregation, and enhance catalytic durability [33]. Nanocages, including MOFs, COFs, porous organic cages, and carbon-based nanocages, offer well-defined cavities, high surface areas, and tunable pore environments that stabilize single atoms and optimize active-site exposure [34–38]. Their structural modularity enables precise adjustment of pore size, functional groups, and electronic environments. Confinement within nanocages enhances SAC stability, prevents agglomeration, and creates microenvironments that modulate reaction pathways and selectivity [39, 40].

Several recent studies highlight the effectiveness of nanocage-supported SACs for NRR. High-throughput DFT screening on d- and p-block metals encapsulated in BN nanocages identified Os@BNNC as a highly active catalyst with a limiting potential of −0.29 V [41]. Metals encapsulated in $B_{36}N_{36}$ nanocages have also demonstrated strong N_2 activation properties under solar-driven conditions [42]. Similarly, Ni@$B_{12}P_{12}$ and Co@$B_{12}P_{12}$ have been identified as stable SACs with promising binding energies and semiconducting behavior [43]. DFT investigations of TM-doped AlN monolayers reveal Os@AlN as an outstanding distal-pathway NRR catalyst with a limiting potential of −0.46 V due to strong N_2 activation [44]. Experimentally, Mo_2C/GaN/InGaN nanowire heterostructures have achieved solar-driven NRR with a Faradaic efficiency of 15 % and an ammonia yield of 7.93 μg cm^{-2} h^{-1}, showcasing the potential of GaN-based photocatalytic systems [45]. The central objective of this thesis is to systematically screen and evaluate transition-metal-doped double nanorings as potential catalysts for

the nitrogen reduction reaction (NRR) via the distal pathway using density functional theory (DFT). The specific aims are: To investigate nitrogen conversion to ammonia via the distal pathway in the presence of single-atom catalysts supported on double nanorings using DFT. To explore how double nanorings enhance stability and catalytic performance of SACs for NRR. To identify the most efficient SAC–nanoring systems for NRR through systematic DFT screening. To compute reaction energy barriers and mechanistic steps associated with NRR on double nanorings. To contribute to the development of a sustainable and energy-efficient alternative to the Haber–Bosch process for green ammonia synthesis. To understand the electronic structure, charge transfer, and orbital interactions between N_2 molecules and SAC-decorated nanorings. To evaluate the structural stability and long-term catalytic durability of SACs anchored on double nanorings for effective nitrogen reduction.

2. METHODS

Computational chemistry is an interdisciplinary field that integrates principles from chemistry, physics, biology, and mathematics to investigate chemical systems through theoretical models and computer-based simulations. As an applied extension of theoretical chemistry, it provides a powerful alternative to experimental investigations by enabling the prediction of molecular structures, energetics, and properties with high precision. Over recent decades, computational chemistry has experienced rapid advancement and has become an indispensable tool for researchers across multiple disciplines. It complements experimental studies, guides the design of functional materials, accelerates drug discovery, and provides mechanistic insights into complex physicochemical phenomena often before laboratory experiments are performed. To achieve these objectives, computational chemistry employs a broad spectrum of numerical techniques. The choice of method depends on the nature of the system and the balance between accuracy and computational cost. Commonly used methodologies include: Molecular mechanics describes atoms as spheres and chemical bonds as springs. The molecular geometry is optimized by minimizing the system's potential energy as determined by bond lengths, angles, torsions, and non-bonded interactions. Due to its computational efficiency, it is suitable for large biomolecules and complex systems. Derived from the Latin *ab initio* ("from the beginning"), these approaches solve the Schrödinger equation using no empirical parameters. Although computationally demanding, ab initio methods especially beyond Hartree Fock provide highly accurate descriptions of molecular wavefunctions and electron distributions. These techniques combine quantum mechanical formalisms with empirically derived parameters to reduce computational cost while retaining reasonable accuracy, serving as an intermediate approach between molecular mechanics and ab initio calculations. DFT has become one of the most widely used electronic-structure methods in physics, chemistry, and materials science. It provides a full quantum-mechanical description of many-body systems at significantly lower computational cost than most wavefunction-based methods. DFT is particularly effective for studying ground-state properties of atoms, molecules, surfaces, and extended solids. Together, these computational methods provide a versatile toolkit for understanding the electronic structure, reactivity, and energetics of chemical systems.

Quantum chemical calculations are commonly performed using atomic units (a.u.), a natural unit system that simplifies the mathematical form of quantum mechanical equations. These units are defined as follows: Bohr (a_0): unit of length, Hartree (E□): unit of energy, **|e|:** unit of electronic charge, m_e: unit of electron mass. The adoption of atomic units eliminates several physical constants from the Schrödinger equation, thereby simplifying expressions and reducing computational complexity.

All density functional theory (DFT) calculations were performed using the Gaussian 09 software package [46]. Geometry optimizations were carried out using the long-range corrected, range-separated hybrid functional ωB97XD, which incorporates empirical dispersion corrections. This functional has been widely validated and is recognized for its accuracy in predicting structural, energetic, and non-covalent interaction properties [48]. A def2-TZVP basis set, augmented systematically with diffuse s and p functions, was employed for initial optimizations of the transition-metal-decorated nanorings. All structures were visualized using the GaussView 5.0 interface.

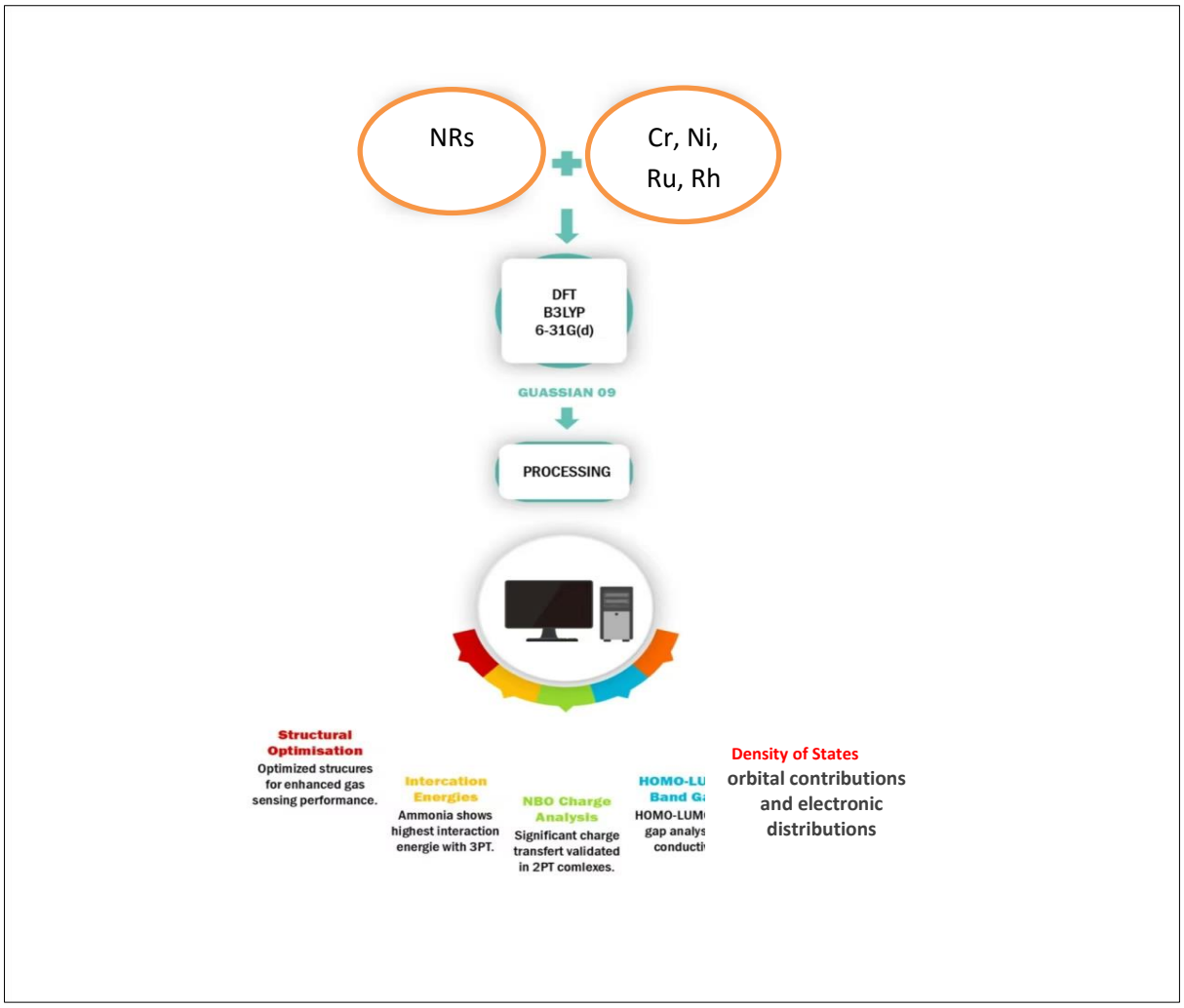

The interaction energies of the transition metal (TM) atoms with the nanorings were computed using the following expressions:

$E_{int} = E_{TM@nanocage} - (E_{nanocage} + E_{TM})$ ---(1)

$E_{int} = E_{total} - (E_{TM@nanocage} + E_{N_2})$ ----------(2)

These equations quantify the binding strength of the metal atom to the nanoring and the interaction energy with adsorbed N_2, respectively. To examine the nitrogen reduction reaction (NRR) pathway over the most stable catalyst ($Ru@B_8N_8$), a mixed basis-set approach was adopted.

- **Ru atom:** Treated using the LANL2DZ effective core potential to account for relativistic effects.
- **B, N, and H atoms:** Described with the 6-31G(d,p) basis set, providing a balance between computational efficiency and accuracy for the nanoring framework. This approach ensures a reliable description of the active catalytic site while maintaining reasonable computational cost.

To gain deeper insight into bonding characteristics and reactivity patterns, the following analyses were performed:

- Natural Bond Orbital (NBO) analysis for charge transfer and donor–acceptor interactions
- Frontier Molecular Orbital (FMO) analysis to determine HOMO–LUMO energy gaps
- Density of States (DOS) calculations to elucidate orbital contributions and electronic distributions

Together, these computational tools provide a comprehensive understanding of the structural stability, electronic properties, and catalytic behavior of transition-metal-supported nanorings toward electrochemical nitrogen reduction.

3. RESULTS AND DISCUSSION

3.1 Optimized Structures of Double Nanorings

In this study, a series of double nanorings were investigated as potential supports for single transition-metal atoms for use in electrochemical nitrogen reduction. Geometry optimizations were performed for the isolated nanorings prior to metal incorporation to evaluate their intrinsic structural characteristics. The

optimized B_8N_8 nanoring exhibits a uniform B–N bond length of 1.45 Å, consistent with the strong covalent character of the B–N linkage. For the B_8P_8 and Ga_8N_8 nanorings, the optimized geometries reveal B–P and Ga–N bond lengths of 1.93 Å and 1.84 Å, respectively. The Al_8N_8 and Al_8P_8 nanorings were likewise optimized, yielding Al–N and Al–P bond lengths of 1.78 Å and 2.29 Å, respectively. These optimized bond lengths confirm the expected periodic trends: bond distances increase with the incorporation of heavier group-13 or group-15 atoms, while lighter combinations (e.g., B–N, Al–N) exhibit shorter and stronger bonding. The optimized geometries serve as the structural foundation for further studies on metal anchoring, interaction energies, and catalytic behavior toward the nitrogen reduction reaction. Showes in fig 1.

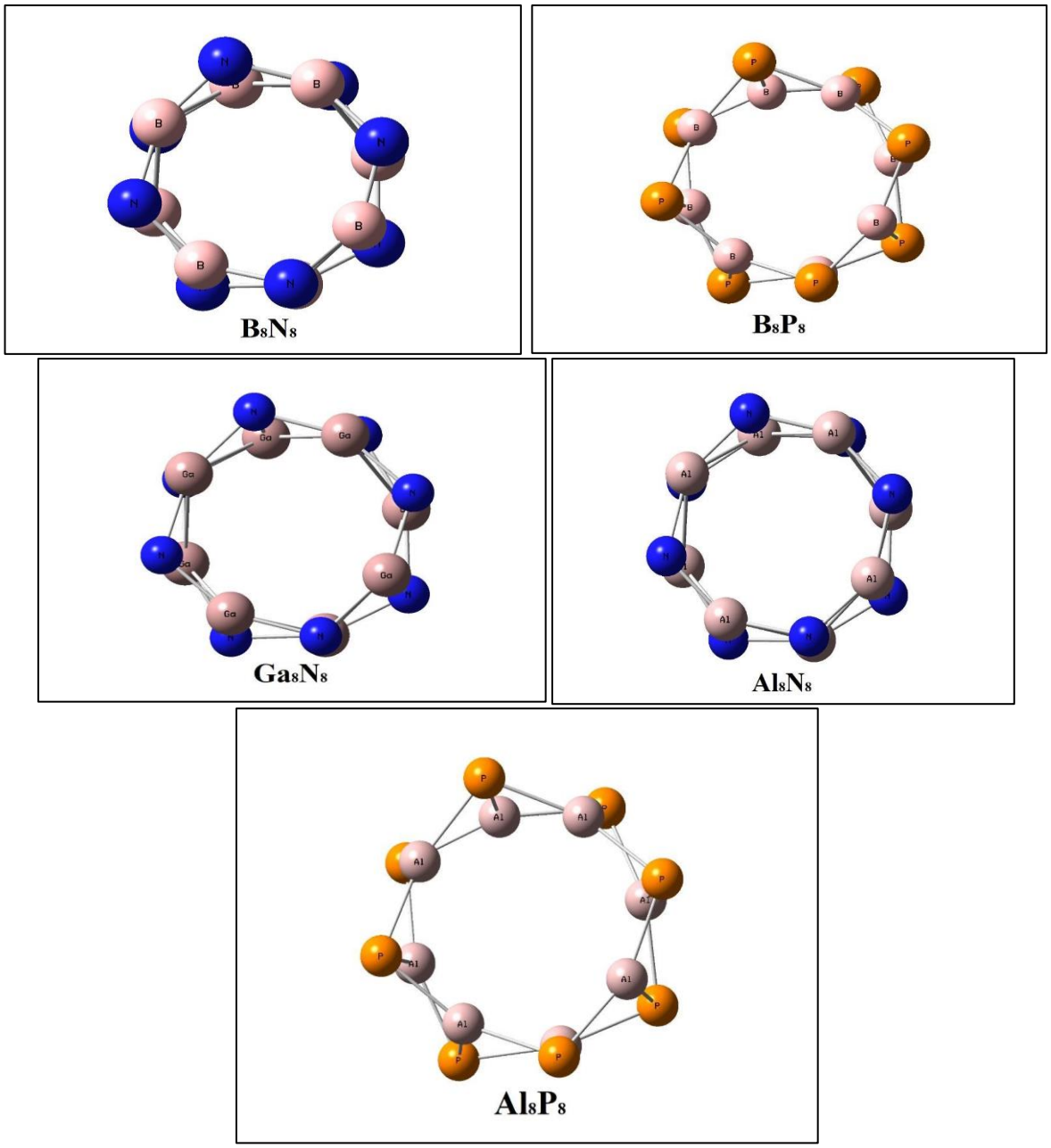

Figure 1: Optimized Structures of Isolated double nanorings

3.2 Optimized Structures of Ru@Nanorings

Multiple initial adsorption geometries were examined to determine the most favorable binding orientation of the Ru atom on each double nanoring. These included placements at the ring center, along the ring edge, and atop individual ring atoms. After full geometry optimization, the lowest-energy configurations were identified for each system. For $Ru@B_8N_8$, the optimized structure shows that the Ru atom coordinates with two boron atoms of the nanoring, with Ru–B bond lengths of approximately 1.99 Å (B_6–Ru_{17} and B_{12}–Ru_{17}). This configuration exhibits a strong interaction energy of −5.784 eV, indicating robust binding and high structural stability. In $Ru@Al_8N_8$, the Ru atom interacts

with two Al atoms, forming Ru–Al bonds of about 2.30 Å (Al_4–Ru_{17} and Al_{12}–Ru_{17}), corresponding to an interaction energy of −4.260 eV. For $Ru@Al_8P_8$, the optimized geometry reveals coordination with four ring atoms two Al and two P atoms with Ru–Al distances of 2.34 Å (Al_6–Ru_{17}, Al_{14}–Ru_{17}) and Ru–P distances of 2.35 Å (P_{10}–Ru_{17}, P_3–Ru_{17}). This structure shows strong binding, with an interaction energy of −5.631 eV. In contrast, $Ru@B_8P_8$ and $Ru@Ga_8N_8$ display significant structural distortion upon optimization, indicating unfavorable binding and reduced stability. These findings suggest that these nanorings are not suitable supports for stabilizing a single Ru atom. Overall, $Ru@B_8N_8$ exhibits the most favorable combination of strong metal support interaction, structural stability, and minimal distortion. Consequently, this system was selected for detailed investigation of the nitrogen reduction reaction mechanism. Showes in fig2.

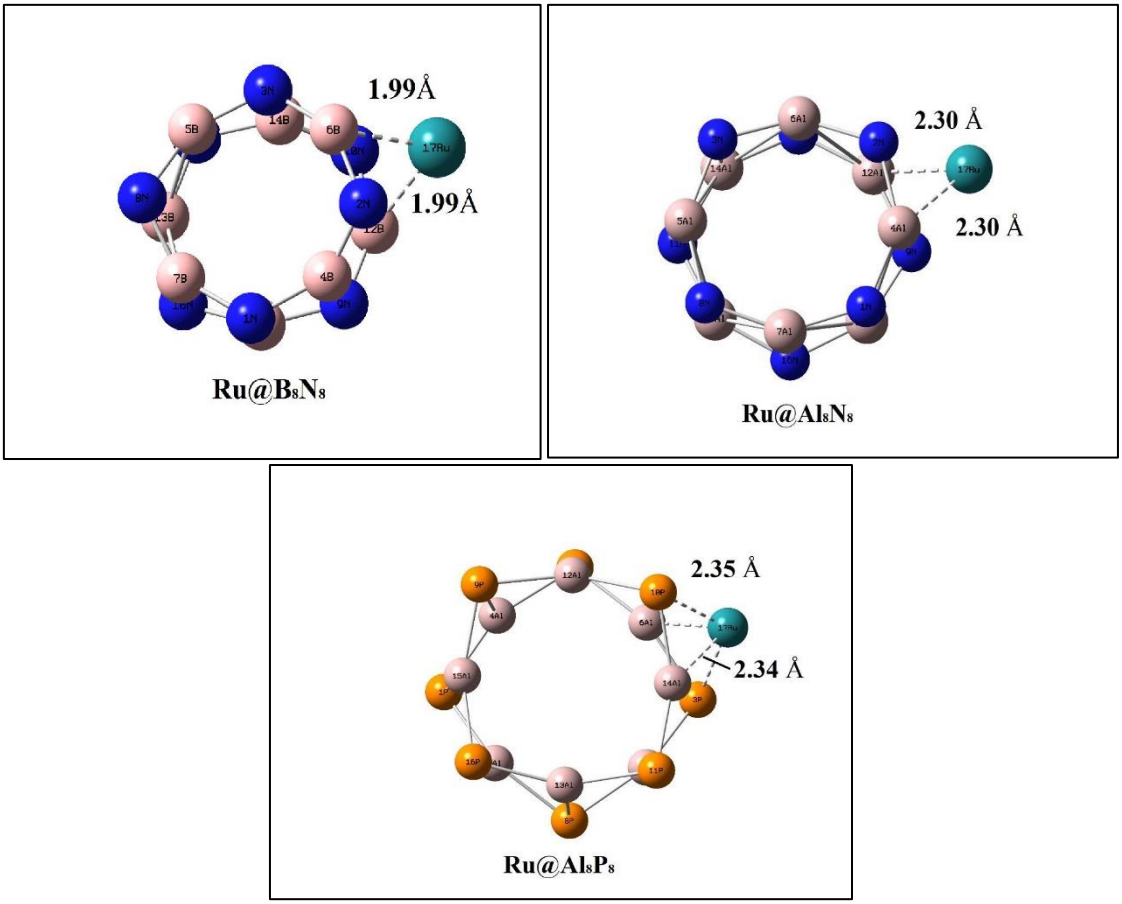

Figure 2: Optimized Structures of Ru@nanorings

3.3 Optimized Structures of Cr@Nanorings

The optimized geometries of the Cr-supported nanorings indicate that chromium exhibits strong and stable interactions with the double nanoring frameworks. For $Cr@B_8N_8$, the Cr atom coordinates with two boron atoms of the ring, with Cr–B bond lengths of approximately 1.98 Å (B_6–Cr_{17} and B_{14}–Cr_{17}), confirming robust binding. In the case of $Cr@B_8P_8$, the optimized structure similarly shows coordination with two boron atoms, yielding Cr–B distances of about 1.94 Å (B_6–Cr_{17} and B_{14}–Cr_{17}). For $Cr@Ga_8N_8$, the Cr atom interacts strongly with a nitrogen atom of the ring, forming a Cr–N bond length of 1.76 Å (N_{10}–Cr_{17}), which is the shortest among the systems studied. This shorter bond length suggests stronger orbital overlap and enhanced stabilization relative to the other nanorings. Overall, the structural optimizations demonstrate that chromium binds effectively to all examined nanorings, with particularly strong interactions observed in $Cr@Ga_8N_8$. Showen in fig3.

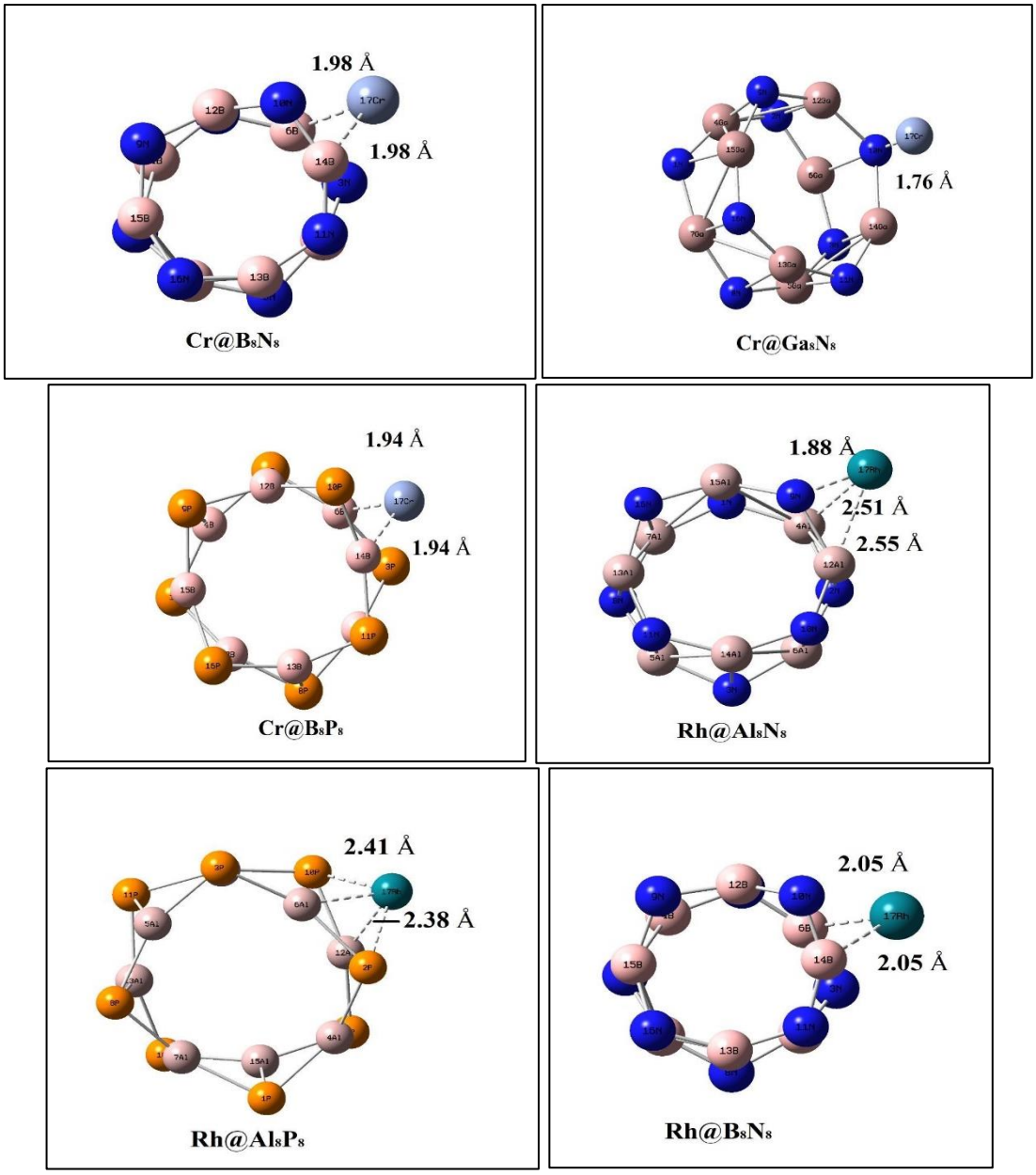

Figure 3: Optimized structure of Cr@nanorings

3.4 Optimized Structures of Ni@Nanorings

The optimized geometries of the Ni-supported nanorings demonstrate that nickel forms stable interactions with all examined double nanoring frameworks. For $Ni@B_8N_8$, the Ni atom coordinates with one boron and one nitrogen atom, exhibiting Ni–B and Ni–N bond lengths of approximately 1.90 Å (B_{12}–Ni_{17}) and 1.77 Å (N_9–Ni_{17}), respectively. In $Ni@B_8P_8$, the optimized structure reveals Ni–B and Ni–P bond distances of 1.91 Å (B_6–Ni_{17}) and 2.10 Å (P_{10}–Ni_{17}), reflecting the larger atomic radius and lower electronegativity of phosphorus. For $Ni@Al_8N_8$, the Ni atom interacts with both an Al and an N atom, forming Ni–Al and Ni–N bonds with lengths of 2.28 Å (Al_{15}–Ni_{17}) and 1.78 Å (N_{16}–Ni_{17}). This combination of long and short bonds indicates mixed ionic–covalent character in the metal–support interaction. In $Ni@Ga_8N_8$, the Ni atom coordinates with Ga and N atoms, with Ni–Ga and Ni–N distances of 2.37 Å (Ga_5–Ni_{17}) and 1.76 Å (N_{10}–Ni_{17}), respectively. Across all systems, the shortest and strongest interactions consistently occur between Ni and nitrogen atoms, while coordination with heavier group-13 atoms (Al, Ga) results in longer, weaker bonds. These optimized geometries confirm that Ni adsorption is structurally feasible on all investigated nanorings, with varying degrees of stabilization depending on the local atomic environment. Showen in fig4.

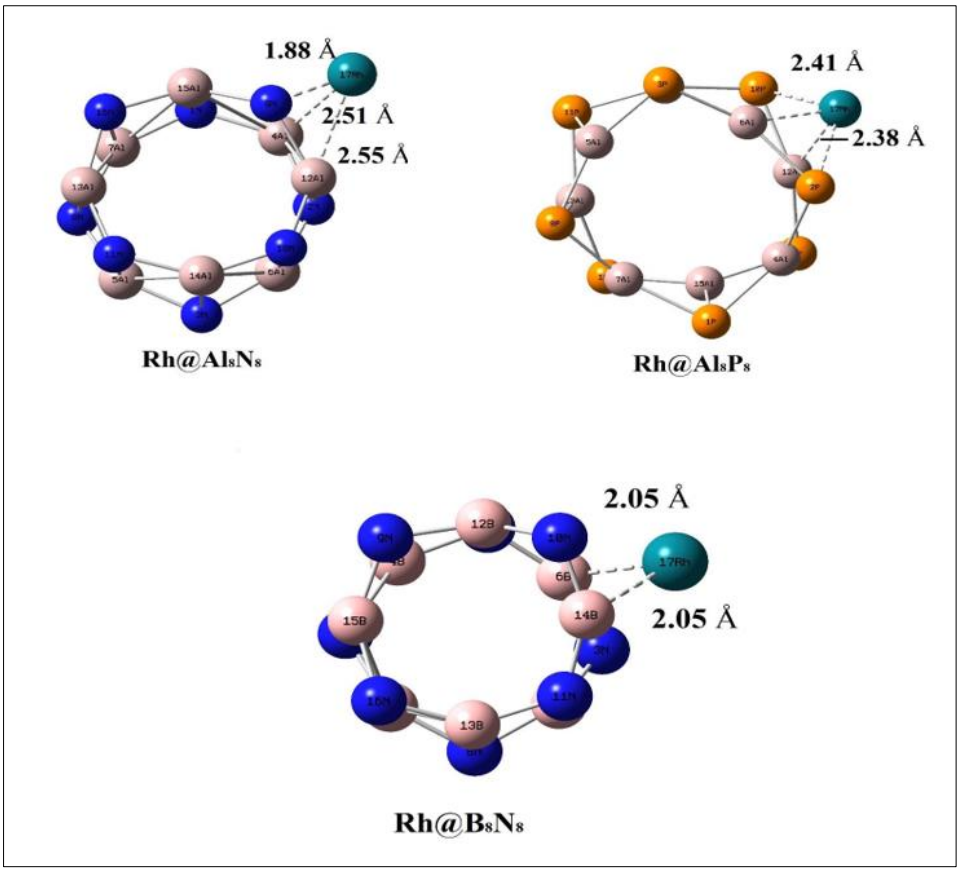

Figure 4: Optimized structures of Ni@nanorings

3.5 Optimized Structures of Rh@Nanorings

The optimized structures of the Rh-supported nanorings show that rhodium interacts stably with all studied frameworks, though with varying coordination environments depending on the atomic composition of the rings. For $Rh@B_8N_8$, the Rh atom binds symmetrically to two boron atoms, with Rh–B bond lengths of approximately 2.05 Å (Rh_{17}–B_6 and Rh_{17}–B_{14}). This coordination indicates moderate metal–support interaction consistent with the electronic characteristics of the B–N network. In $Rh@Al_8N_8$, the optimized geometry reveals that Rh forms two longer Rh–Al bonds 2.51 Å (Al_4–Rh_{17}) and 2.54 Å (Al_{12}–Rh_{17}) along with a shorter Rh–N bond of 1.88 Å (N_9–Rh_{17}). The significant difference in bond lengths suggests stronger orbital overlap with nitrogen relative to aluminum, consistent with the higher electronegativity and better π-donation ability of nitrogen. For $Rh@Al_8P_8$, the Rh atom interacts with both P and Al atoms, forming Rh–P bonds of 2.41 Å (P_{10}–Rh_{17} and P_2–Rh_{17}) and Rh–Al bonds of 2.38 Å (Al_5–Rh_{17} and Al_{12}–Rh_{17}). These bond lengths indicate a mixed coordination environment, with moderately strong stabilization arising from both phosphorus and aluminum donors. Overall, the optimized structures reveal that Rh forms stable interactions across all nanorings, with the shortest and strongest bonds typically observed for Rh–N interactions. The variation in Rh–support bonding reflects the influence of ring composition on metal anchoring and potential catalytic behavior. Showen in fig5.

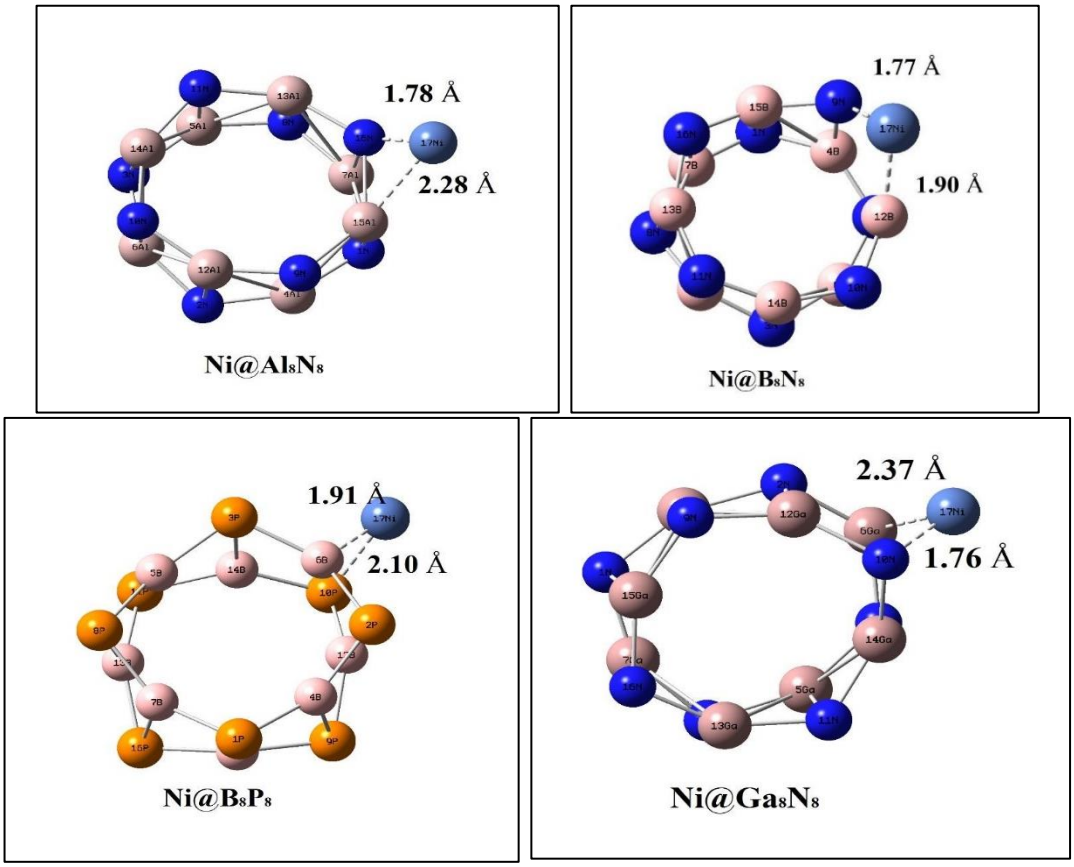

Figure 5: Optimized structures of Ni@nanorings

3.6 Interaction Energies of TM@Nanorings

The interaction energies of four transition-metal atoms (Ru, Rh, Cr, and Ni) with five double nanorings B_8N_8, B_8P_8, Al_8N_8, Al_8P_8, and Ga_8N_8 were computed by evaluating multiple adsorption orientations for each TM–nanoring combination. These interaction energies provide critical insight into the binding strength, stability, and feasibility of metal anchoring on the nanoring frameworks. Across all systems, the interaction energies demonstrate substantial variation depending on both the identity of the metal atom and the atomic composition of the supporting nanoring. Among the configurations studied, $Ru@B_8N_8$ exhibits the most favorable (largest negative) interaction energy, indicating exceptionally strong metal support binding and high thermodynamic stability. This strong stabilization is consistent with the optimized structural analysis, which showed robust Ru–B coordination and minimal structural distortion upon adsorption. In contrast, certain systems such as $Ru@B_8P_8$ and $Ru@Ga_8N_8$ displayed weaker binding and noticeable geometric deformation, suggesting poor stabilization of the metal atom. Similar trends were observed for other TMs: strong binding typically occurred when the metal coordinated with nitrogen-rich environments, while heavier group-13 and group-15 atoms provided less effective stabilization. Because $Ru@B_8N_8$ demonstrated the most favorable interaction energy among all TM@nanoring systems examined, it was selected as the active catalyst model for detailed investigation of the electrochemical nitrogen reduction reaction (NRR) mechanism shows in table1.

Table 1: Interaction energies of TM@nanorings

Complex	Orientation 1: Center Eint (Ev)	Orientation 2: Side Eint (Ev)	Orientation 3	Eint (Ev)	Orientation 4	Eint (Ev)
Cr@Ga8N8	-8.381	-8.290	Above N	-5.368	Above Ga	-
Cr@Al8P8	-7.534	-5.157	Above Al	-	Above P	-2.328
Cr@Al8N8	-3.786	-5.419	Above Al	-	Above N	-5.903
Cr@B8P8	-7.614	-6.383	Above B	-	Above P	-
Cr@B8N8	0.561	-5.953	Above B	-	Above N	-
Ni@Ga8N8	-1.873	-4.145	Above N	-4.141	Above Ga	-4.141
Ni@Al8P8	-4.400	-3.802	Above Al	-3.547	Above P	-3.547

Ni@Al8N8	-1.456	-3.705	Above Al	-1.456	Above N	-3.818
Ni@B8P8	-4.629	-3.602	Above B	-3.56	Above P	-3.560
Ni@B8N8	2.602	-3.059	Above B	-3.27	Above N	-3.273
Ru@Ga8N8	-2.386	-5.147	Above N	-7.278	Above Ga	-
Ru@Al8P8	-7.939	-5.631	Above Al	-	Above P	-
Ru@Al8N8	-1.687	-4.260	Above Al	-4.765	Above N	-4.765
Ru@B8P8	-7.053	-6.693	Above B	-	Above P	-
Ru@B8N8	-0.774	-5.784	Above B	-	Above N	-5.784
Rh@Ga8N8	-	-	Above N	-	Above Ga	-
Rh@Al8P8	-4.282	-3.798	Above Al	-3.425	Above P	-
Rh@Al8N8	-	-2.447	Above Al	-	Above N	-
Rh@B8P8	-4.093	-4.510	Above B	-4.510	Above P	-
Rh@B8N8	-1.304	-3.739	Above B	-	Above N	-

3.7 Global Reactivity Descriptors

To achieve a deeper understanding of the electronic behavior, reactivity, and intrinsic stability of the catalyst systems, a series of global reactivity descriptors were evaluated using frontier molecular orbital (FMO) theory. These descriptors—derived from the energies of the highest occupied molecular orbital (HOMO) and lowest unoccupied molecular orbital (LUMO)—include the ionization potential (VIP), electron affinity (VEA), chemical hardness (η), softness (S), chemical potential (μ), Fermi level, electrophilicity index (ω), electronegativity (χ), and the HOMO–LUMO energy gap. Collectively, these parameters provide valuable insight into the electronic characteristics that govern catalytic performance toward the nitrogen reduction reaction (NRR). The ionization potential (VIP) and electron affinity (VEA) were obtained from vertical energy differences and serve as the foundation for calculating other global descriptors. Chemical hardness (η), defined as half the energy difference between the HOMO and LUMO levels, measures the resistance of a system to electronic deformation:

$$\eta = \frac{VIP-VEA}{2}$$

A larger η value reflects greater molecular stability and reduced chemical reactivity. In contrast, softness (S), the reciprocal of chemical hardness, quantifies the ease with which a molecule can undergo charge redistribution an essential property in catalytic steps such as N_2 adsorption and activation:

$$S = 1/2\eta$$

The chemical potential (μ), which describes the escaping tendency of electrons from a system, was calculated using:

$$\eta = \frac{-(VIP-VEA)}{2}$$

Since the chemical potential is numerically equivalent to the Fermi level, it indicates the electronic equilibrium point where the probability of electron occupation is 50%. This descriptor is crucial for understanding electron flow between the active site and the adsorbed N_2 molecule. The electrophilicity index (ω), which evaluates the system's ability to accept electrons, was computed from μ and η according to:

$$\omega = \mu 2/2\eta$$

Higher ω values signify stronger electrophilic behavior, which enhances the interaction of the catalyst with nitrogen molecules by facilitating electron acceptance and subsequent activation. The HOMO–LUMO energy gap serves as an indicator of kinetic stability and overall chemical reactivity. A smaller energy gap implies enhanced charge-transfer capability and increased reactivity—attributes that are generally favorable for NRR catalysis. Finally, electronegativity (χ), representing the tendency of a system to attract electrons, is related to chemical potential by $\chi = -\mu$. Moderate electronegativity values promote effective electron donation from the metal center to the adsorbed N_2 molecule, enabling its activation and facilitating subsequent reduction steps showa in table 2 and 3.

Table 2: Calculated values of reactivity parameters

Complex	HOMO (eV)	LUMO (eV)	Ionization Potential (VIP, eV)	Electron Affinity (VEA, eV)	Chemical Hardness (η, eV)	Softness (S, eV^{-1})
B8P8+Cr CENTRE	-7.619	-1.817	7.619	1.817	2.901	0.172
B8P8+Cr SIDE	-7.863	-1.565	7.863	1.565	3.149	0.159
B8P8+Cr WB	–	–	–	–	–	–
B8P8+Cr WP	–	–	–	–	–	–
B8N8+Cr CENTRE	-7.070	-0.403	7.070	0.403	3.333	0.150
B8N8+Cr SIDE	-7.228	-0.416	7.228	0.416	3.406	0.147
B8N8+Cr WB	-0.170	-0.559	0.170	0.559	-0.194	-2.571
B8N8+Cr WN	–	–	–	–	–	–
Al8N8+Cr CENTRE	-5.641	-1.022	5.641	1.022	2.310	0.216

Complex	HOMO (eV)	LUMO (eV)	Ionization Potential (VIP, eV)	Electron Affinity (VEA, eV)	Chemical Hardness (η, eV)	Softness (S, eV^{-1})
Al8N8+Cr SIDE	-7.281	-0.620	7.281	0.620	3.330	0.150
Al8N8+Cr WAL	–	–	–	–	–	–
Al8N8+Cr WN	-7.606	-0.821	7.606	0.821	3.393	0.147
Al8P8+Cr CENTRE	-6.904	-1.832	6.904	1.832	2.536	0.197
Al8P8+Cr SIDE	-6.919	-1.481	6.919	1.481	2.719	0.184
Al8P8+Cr WAL	–	–	–	–	–	–
Al8P8+Cr WP	-6.804	-2.001	6.804	2.001	2.401	0.208
Ga8N8+Cr CENTRE	-7.648	-2.217	7.648	2.217	2.716	0.184
Ga8N8+Cr SIDE	-7.787	-1.433	7.787	1.433	3.177	0.157
Ga8N8+Cr WGA	–	–	–	–	–	–
Ga8N8+Cr WN	-7.192	-1.478	7.192	1.478	2.857	0.175
B8P8+Rh CENTRE	-7.551	-2.100	7.551	2.100	2.725	0.183
B8P8+Rh SIDE	-1.734	-7.417	1.734	7.417	-2.842	-0.176
B8P8+Rh WB	-7.417	-1.733	7.417	1.733	2.842	0.176
B8P8+Rh WP	–	–	–	–	–	–
B8N8+Rh CENTRE	-7.787	-0.560	7.787	0.560	3.613	0.138
B8N8+Rh SIDE	-8.096	-0.507	8.096	0.507	3.795	0.132
B8N8+Rh WB	-6.844	-0.509	6.844	0.509	3.167	0.158
B8N8+Rh WN	-6.753	-0.446	6.753	0.446	3.153	0.159
Al8N8+Rh CENTRE	-7.437	-1.017	7.437	1.017	3.210	0.156
Al8N8+Rh SIDE	-7.780	-0.828	7.780	0.828	3.476	0.144
Al8N8+Rh WAL	–	–	–	–	–	–
Al8N8+Rh WN	-7.444	-1.228	7.444	1.228	3.108	0.161
Al8P8+Rh CENTRE	-7.330	-1.695	7.330	1.695	2.818	0.177
Al8P8+Rh SIDE	-7.133	-1.632	7.133	1.632	2.751	0.182
Al8P8+Rh WAL	-7.099	-1.756	7.099	1.756	2.671	0.187
Al8P8+Rh WP	–	–	–	–	–	–
Ga8N8+Rh CENTRE	-7.152	-1.982	7.152	1.982	2.585	0.193
Ga8N8+Rh SIDE	-7.341	-1.826	7.341	1.826	2.758	0.181
Ga8N8+Rh WGA	–	–	–	–	–	–
Ga8N8+Rh WN	–	–	–	–	–	–
B8P8+Ru CENTRE	-8.031	-1.934	8.031	1.934	3.048	0.164
B8P8+Ru SIDE	-7.716	-1.596	7.716	1.596	3.060	0.163
B8P8+Ru WB	–	–	–	–	–	–
B8P8+Ru WP	–	–	–	–	–	–
B8N8+Ru CENTRE	-7.709	-0.983	7.709	0.983	3.363	0.149
B8N8+Ru SIDE	-7.943	-0.478	7.943	0.478	3.733	0.134
B8N8+Ru WB	–	–	–	–	–	–
B8N8+Ru WN	-7.943	-0.477	7.943	0.477	3.733	0.134
Al8N8+Ru CENTRE	-6.434	-1.248	6.434	1.248	2.593	0.193
Al8N8+Ru SIDE	-6.886	-0.730	6.886	0.730	3.078	0.162
Al8N8+Ru WAL	-7.240	-1.639	7.240	1.639	2.801	0.179
Al8N8+Ru WN	-7.241	-1.638	7.241	1.638	2.801	0.178
Al8P8+Ru SIDE	-7.189	-1.528	7.189	1.528	2.831	0.177
Al8P8+Ru WAL	–	–	–	–	–	–
Al8P8+Ru WP	–	–	–	–	–	–
Ga8N8+Ru CENTRE	–	–	–	–	–	–
Ga8N8+Ru SIDE	-6.893	-2.049	6.893	2.049	2.422	0.206
Ga8N8+Ru WGA	–	–	–	–	–	–
Ga8N8+Ru WN	-6.893	-2.049	6.893	2.049	2.422	0.206
Ga8N8+Ni CENTRE	-7.549	-2.105	7.549	2.105	2.722	0.184
Ga8N8+Ni SIDE	-8.070	-1.669	8.070	1.669	3.201	0.156
Ga8N8+Ni WGA	-7.973	-1.723	7.973	1.723	3.125	0.160

Table 3: Calculated values reactivity parameters

Complex	Chemical Potential (μ, eV)	Fermi Level (EFL, eV)	Electrophilicity Index (ω, eV)	HOMO–LUMO Gap (eV)
B8P8+Cr CENTRE	-4.718	-4.718	3.837	5.802
B8P8+Cr SIDE	-4.714	-4.714	3.528	6.299
B8P8+Cr WB	–	–	–	–
B8P8+Cr WP	–	–	–	–
B8N8+Cr CENTRE	-3.737	-3.737	2.094	6.667
B8N8+Cr SIDE	-3.822	-3.822	2.144	6.813
B8N8+Cr WB	-0.365	-0.365	-0.342	-0.389
B8N8+Cr WN	–	–	–	–
Al8N8+Cr CENTRE	-3.331	-3.331	2.402	4.620
Al8N8+Cr SIDE	-3.950	-3.950	2.343	6.661
Al8N8+Cr WAL	–	–	–	–
Al8N8+Cr WN	-4.214	-4.214	2.617	6.785
Al8P8+Cr CENTRE	-4.368	-4.368	3.761	5.072
Al8P8+Cr SIDE	-4.200	-4.200	3.244	5.438
Al8P8+Cr WAL	–	–	–	–
Al8P8+Cr WP	-4.402	-4.402	4.036	4.802
Ga8N8+Cr CENTRE	-4.932	-4.932	4.479	5.432
Ga8N8+Cr SIDE	-4.610	-4.610	3.345	6.354
Ga8N8+Cr WGA	–	–	–	–
Ga8N8+Cr WN	-4.335	-4.335	3.289	5.713
B8P8+Rh CENTRE	-4.825	-4.825	4.271	5.451
B8P8+Rh SIDE	-4.575	-4.575	-3.684	-5.683
B8P8+Rh WB	-4.575	-4.575	3.683	5.684
B8P8+Rh WP	–	–	–	–
B8N8+Rh CENTRE	-4.173	-4.173	2.410	7.227
B8N8+Rh SIDE	-4.302	-4.302	2.438	7.589
B8N8+Rh WB	-3.676	-3.676	2.134	6.334
B8N8+Rh WN	-3.600	-3.600	2.055	6.307
Al8N8+Rh CENTRE	-4.227	-4.227	2.783	6.420
Al8N8+Rh SIDE	-4.304	-4.304	2.665	6.952
Al8N8+Rh WAL	–	–	–	–
Al8N8+Rh WN	-4.336	-4.336	3.025	6.216
Al8P8+Rh CENTRE	-4.513	-4.513	3.614	5.635
Al8P8+Rh SIDE	-4.382	-4.382	3.491	5.502
Al8P8+Rh WAL	-4.427	-4.427	3.668	5.343
Al8P8+Rh WP	–	–	–	–
Ga8N8+Rh CENTRE	-4.567	-4.567	4.034	5.170
Ga8N8+Rh SIDE	-4.584	-4.584	3.809	5.515
Ga8N8+Rh WGA	–	–	–	–
Ga8N8+Rh WN	–	–	–	–
B8P8+Ru CENTRE	-4.983	-4.983	4.072	6.097
B8P8+Ru SIDE	-4.656	-4.656	3.542	6.121
B8P8+Ru WB	–	–	–	–
B8P8+Ru WP	–	–	–	–
B8N8+Ru CENTRE	-4.346	-4.346	2.808	6.726
B8N8+Ru SIDE	-4.211	-4.211	2.375	7.465
B8N8+Ru WB	–	–	–	–
B8N8+Ru WN	-4.210	-4.210	2.374	7.466
Al8N8+Ru CENTRE	-3.841	-3.841	2.844	5.186
Al8N8+Ru SIDE	-3.808	-3.808	2.356	6.155
Al8N8+Ru WAL	-4.439	-4.439	3.519	5.601
Al8N8+Ru WN	-4.440	-4.440	3.518	5.603
Al8P8+Ru CENTRE	-4.610	-4.610	3.923	5.418
Al8P8+Ru SIDE	-4.358	-4.358	3.355	5.662

Complex	Chemical Potential (μ, eV)	Fermi Level (EFL, eV)	Electrophilicity Index (ω, eV)	HOMO–LUMO Gap (eV)
Al8P8+Ru WAL	–	–	–	–
Al8P8+Ru WP	–	–	–	–
Al8N8+Ni SIDE	-4.246	-4.246	2.588	6.967
Al8N8+Ni WAL	-4.182	-4.182	2.566	6.817
Al8N8+Ni WN	-4.183	-4.183	2.566	6.818
Al8P8+Ni CENTRE	-4.607	-4.607	3.735	5.683
Al8P8+Ni SIDE	-4.448	-4.448	3.592	5.507
Al8P8+Ni WAL	-4.781	-4.781	3.722	6.142
Al8P8+Ni WP	-4.781	-4.781	3.722	6.142
Al8N8	-4.653	-4.653	2.896	7.474
Al8P8	-5.010	-5.010	3.955	6.346
B8N8	-4.804	-4.804	2.130	10.835
B8P8	-5.325	-5.325	4.341	6.533
Ga8N8	-5.169	-5.169	4.231	6.313

3.8 NRR Mechanism: Distal Pathway

In this study, the distal pathway was investigated for the electrochemical nitrogen reduction reaction (NRR) using Ru@B8N8 as the catalytic center. In this mechanism, the two nitrogen atoms of the adsorbed N_2 molecule are hydrogenated sequentially. The nitrogen atom farther from the catalyst surface, referred to as the *distal nitrogen*, is first protonated and reduced to form the first ammonia molecule (NH_3), which subsequently desorbs from the catalyst surface. Following this shows in fig6, the proximal nitrogen, which is directly bonded to the Ru atom, undergoes successive hydrogenation to generate the second ammonia molecule, completing the NRR process. The TM@nanocage structure provides a highly stable and confined environment that anchors the transition metal atom, maintaining its isolation and catalytic activity. This single-atom catalytic center efficiently adsorbs and activates the N_2 molecule by weakening the strong N≡N triple bond, facilitating stepwise hydrogenation along the distal pathway.

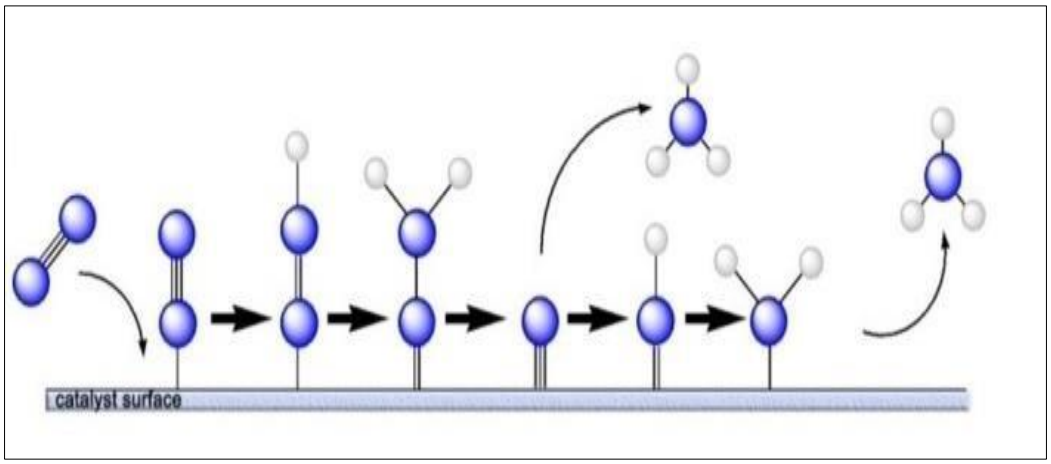

Figure 6: Distil Pathway Scheme

3.9 Interaction Energies of NRR Intermediates on Ru@B8N8

The interaction energies (Eint) of key nitrogen reduction reaction (NRR) intermediates on the Ru@B8N8 catalyst were calculated to evaluate their adsorption strength and relative stability during the reaction pathway. In general, more negative interaction energies correspond to stronger adsorption and greater stabilization on the catalytic surface. The results reveal that molecular nitrogen (N_2) exhibits the weakest interaction with an Eint_\text{int}int of –1.879 eV, indicating physisorption at the Ru active site. In contrast, the atomic nitrogen (N) intermediate shows the strongest adsorption, with an interaction energy of –10.27 eV, reflecting strong chemisorption and significant stabilization after N≡N bond cleavage. As hydrogenation proceeds, species such as N_2H (–4.551 eV), NNH_2 (–6.471 eV), and NH (–8.818 eV) display progressively stronger binding, demonstrating the catalyst's ability to effectively stabilize partially hydrogenated intermediates [49-52]. Importantly, the final product NH_3 binds with a comparatively weaker interaction energy of –2.973 eV, which is advantageous for facile desorption and product release which showa in table4. Overall, these interaction energy trends confirm that Ru@B8N8 provides an optimal balance between sufficiently activating the

adsorbed N_2 molecule and enabling the efficient desorption of NH_3. This balance underscores the potential of Ru@B8N8 as an efficient single-atom catalyst for the nitrogen reduction reaction.

Table 4: Interaction energies, QNBO HOMO-LUMO, of NRR intermediates@RuB_8N_8

Complex	Eint (eV)	QNBO Charge (e)	HOMO (eV)	LUMO (eV)	HOMO–LUMO Gap (eV)
B8N8 (bare)	–	–	–7.39	2.88	4.50
Ru@B8N8 (clean surface)	–	–	–5.01	1.65	3.36
N_2@RuB8N8	–1.879	–0.100	–5.41	0.88	4.53
N_2H@RuB8N8	–4.551	–0.188	–6.32	1.31	5.01
NNH_2@RuB8N8	–6.471	–0.007	–5.39	1.97	3.42
N@RuB8N8	–10.27	–0.109	–6.52	1.32	5.20
NH@RuB8N8	–8.818	–0.155	–5.99	1.40	4.59
NH_2@RuB8N8	–4.946	–0.093	–4.81	1.52	3.29
NH_3@RuB8N8	–2.973	+0.284	–4.30	2.43	1.87

3.10 NBO (QNBO) Analysis

Charge transfer plays a crucial role in determining how effectively the catalyst interacts with the nitrogen reduction intermediates. To quantify the electronic exchange between the Ru@B8N8 active site and each adsorbed species, a Natural Bond Orbital (NBO) analysis was performed. In this context, negative charge transfer values indicate electron donation from the catalyst to the intermediate**,** while positive values represent electron back-donation or electron withdrawal from the catalyst surface**.** The results reveal that early-stage intermediates such as N_2 and N_2H exhibit relatively small charge transfer values, consistent with their weaker activation on the catalytic surface. As the reaction progresses and the N≡N bond becomes increasingly weakened, intermediates like NNH_2, NH, and atomic N display significantly larger charge transfer values. This reflects stronger electronic interactions, enhanced orbital overlap, and effective stabilization of these species by the Ru active site. For the final product NH_3, the charge transfer magnitude decreases noticeably, implying weaker electronic interaction with the catalyst. This reduced charge exchange facilitates desorption of NH_3, which is essential for catalyst regeneration and continuous turnover showa in table4. Overall, the QNBO analysis confirms that Ru@B8N8 provides an electronically favorable environment for the activation of N_2 and the stabilization of hydrogenated intermediates while simultaneously enabling easy release of the final ammonia product.

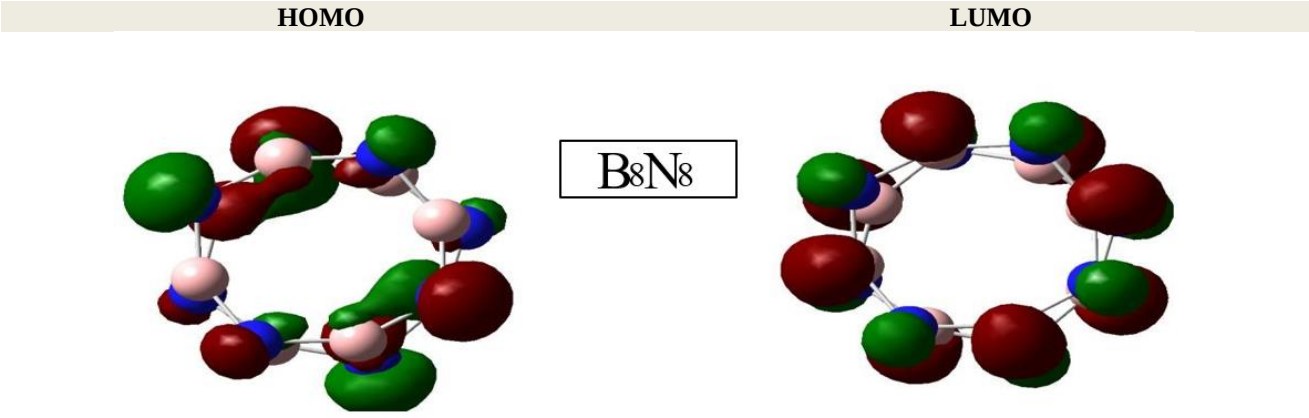

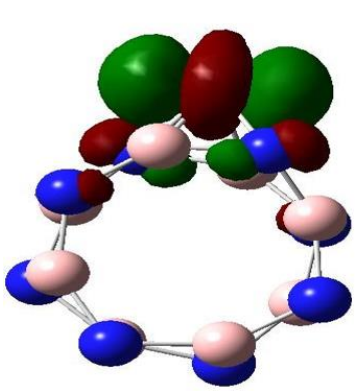

$Ru@B_8N_8$

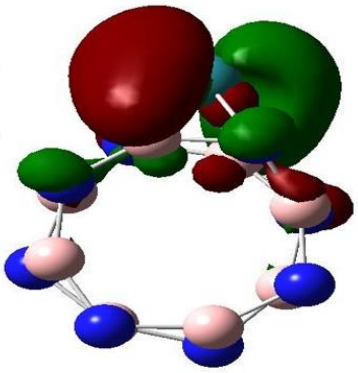

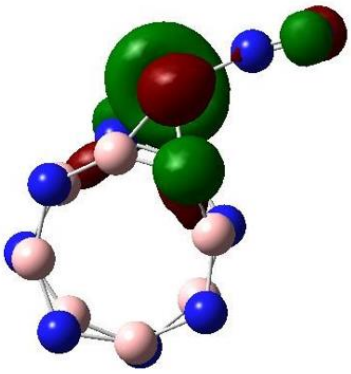

$N_2@RuB_8N_8$

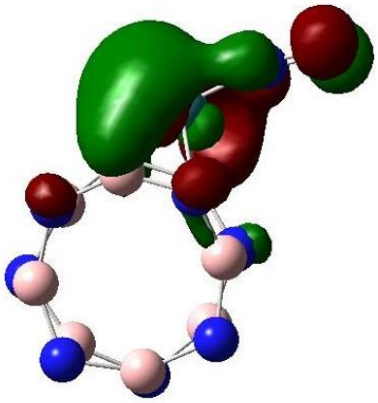

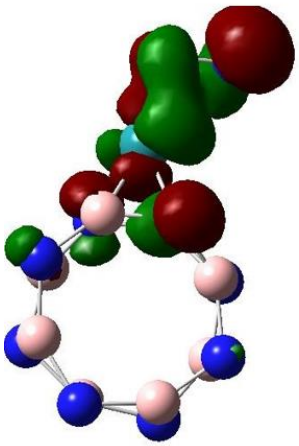

$N_2H@RuB_8N_8$

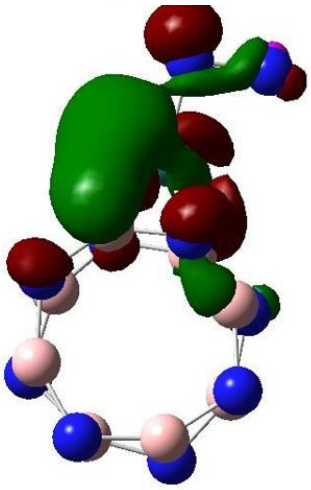

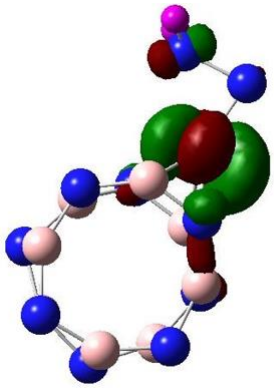

$NNH@RuB_8N_8$

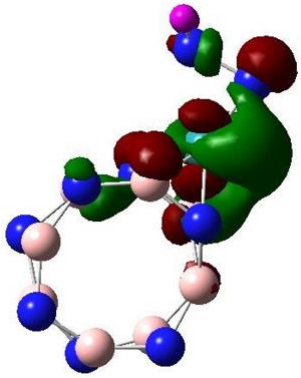

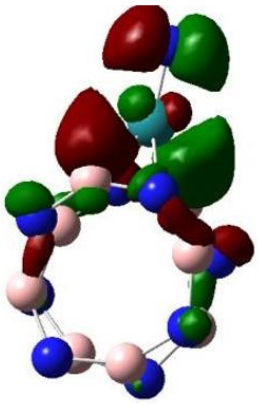

$N@RuB_8N_8$

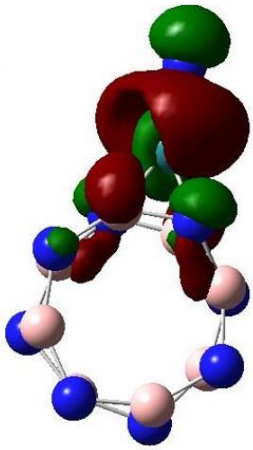

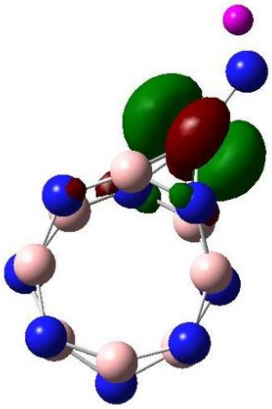

$NH@RuB_8N_8$

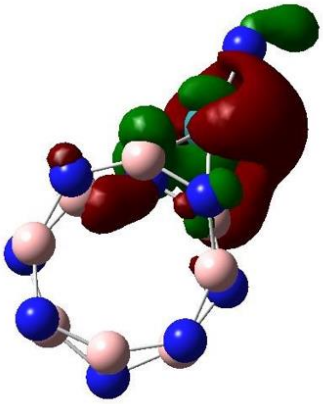

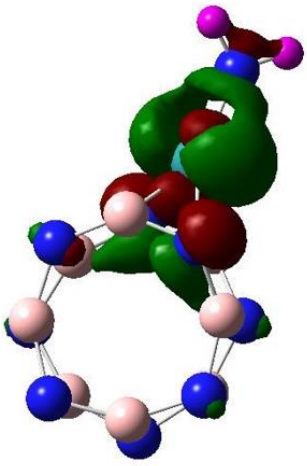

$NH_2@RuB_8N_8$

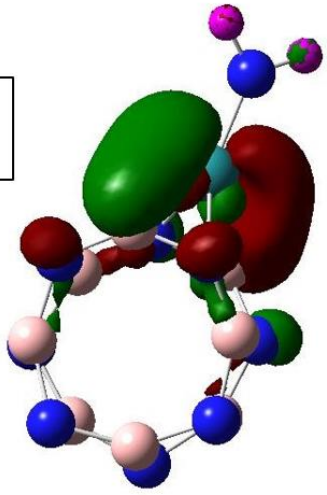

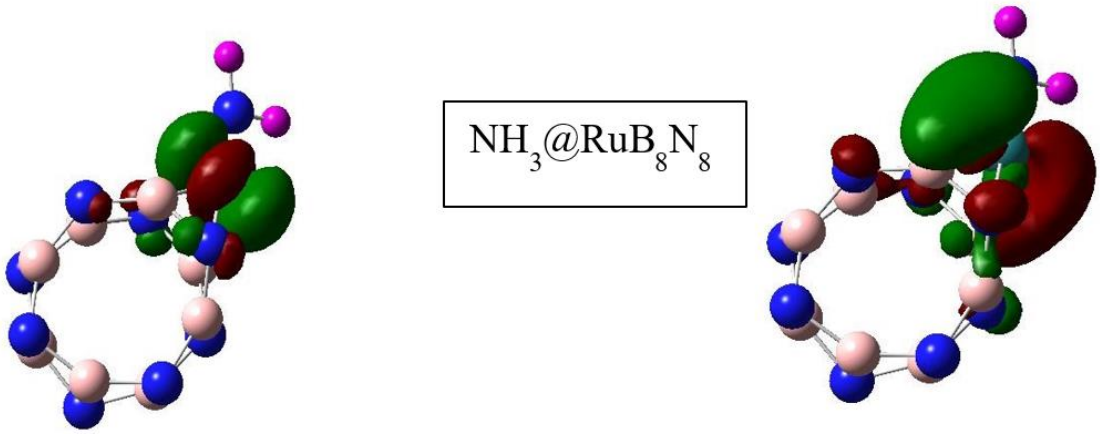

Figure 9: HOMO and LUMO Surfaces of NRR intermediates@RuB_8N_8

3.11 density of states (dos) analysis

Density of States (DOS) analysis provides critical insight into the electronic behavior of catalytic systems by revealing how energy levels are distributed and how peak intensities evolve during interaction with reactants and intermediates. Variations in DOS peaks reflect changes in electronic transport, which can enhance or diminish conductivity and directly influence catalytic performance. For the Ru-supported B_8N_8 nanoring, the DOS spectra of all nitrogen reduction reaction (NRR) intermediates along the distal pathway exhibit a consistent electronic framework. The occupied states are mainly distributed between –10 eV and –4 eV, originating from hybridization between Ru-4d and B/N-2p orbitals, confirming stable bonding interactions at the active site. The virtual states appearing above 2 eV indicate available channels for electron acceptance during proton–electron transfer steps. In the initial N_2@RuB_8N_8 adsorption complex, the DOS profile shows a relatively large HOMO–LUMO separation (~5.5–6 eV). This wide gap indicates insulating character, which is beneficial for selective activation of N_2. Electron donation from Ru to the antibonding π^* orbitals of N_2 weakens the N≡N triple bond, initiating the reduction process. Upon formation of N_2H@RuB_8N_8, new states emerge closer to the Fermi level (0 eV), reflecting enhanced electronic activity that facilitates the first protonation step. The system maintains an adequate energy gap, ensuring structural stability. For the NNH_2@RuB_8N_8 intermediate, additional DOS intensity appears near the Fermi level due to increased hydrogenation, while the presence of virtual states suggests continued ability to accept electrons during subsequent reduction steps. In the N@RuB_8N_8 intermediate, significant DOS peaks develop in both occupied and virtual regions. The increase in DOS around 0 eV corresponds to strong chemisorption of the atomic nitrogen, enabling efficient protonation toward NH formation. The NH@RuB_8N_8 spectrum features a pronounced DOS peak near the Fermi level and a rich distribution of virtual states, highlighting a favorable environment for further hydrogenation. Similarly, NH_2@RuB_8N_8 exhibits an increased DOS density near 0 eV, reflecting stronger orbital interactions involving the NH_2 group and the Ru center. The maintained energy gap (~5–6 eV) supports both reactivity and system stability. Finally, the NH_3@RuB_8N_8 spectrum shows a decrease in DOS intensity around the Fermi level and fewer virtual states, consistent with weakened interaction and electron demand as ammonia approaches desorption. This confirms that NH_3 is weakly bound and readily released an essential requirement for an efficient NRR catalyst. Overall, the DOS analysis demonstrates that Ru@B_8N_8 effectively modulates electronic density throughout all NRR intermediates. This dynamic orbital behavior provides the optimal combination of N_2 activation, stabilization of protonated species, and facile NH_3 desorption, supporting the high catalytic potential of Ru@B_8N_8 for the nitrogen reduction reaction.

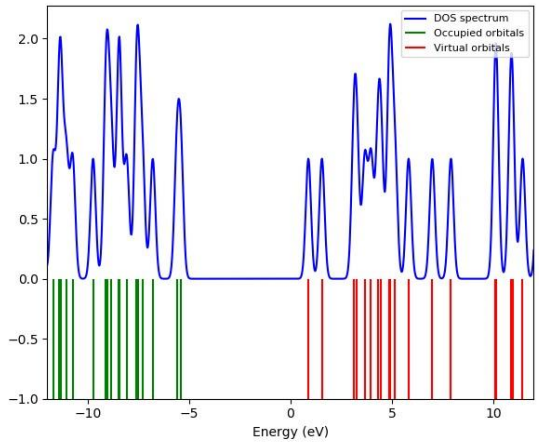

$N_2@RuB_8N_8$

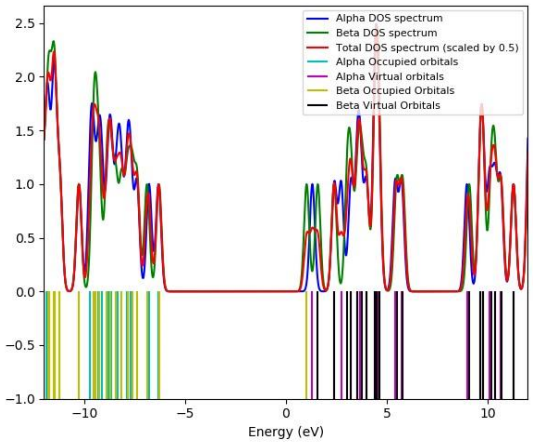

$N_2H@RuB_8N_8$

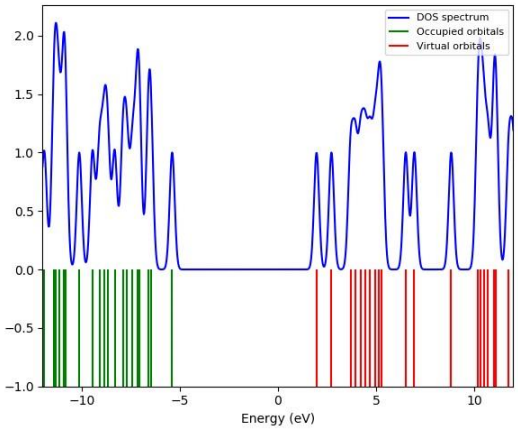

$NNH_2@RuB_8N_8$

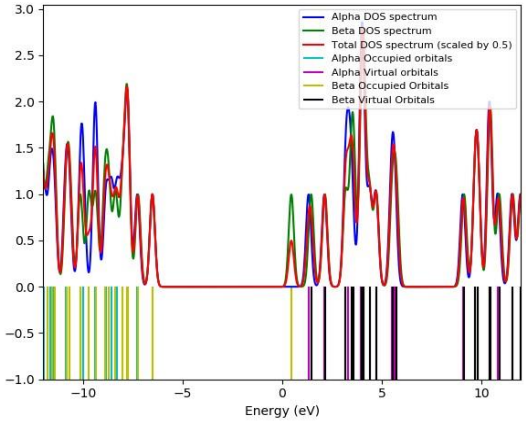

$N@RuB_8N_8$

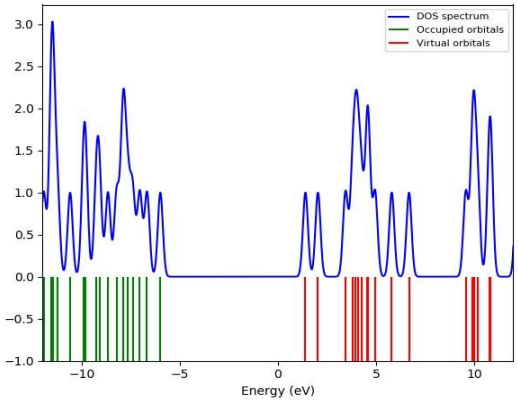

$NH@RuB_8N_8$

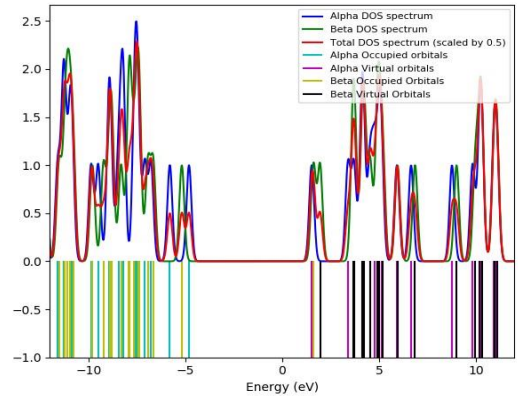

$NH_2@RuB_8N_8$

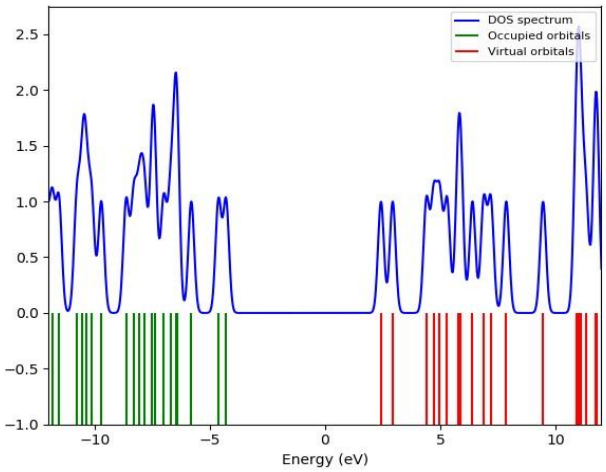

NH_3@RuB8N_8

Figure 15: DOS Spectra of N_2, N_2H, NNH_2, N, NH, NH_2, NH_3@RuB8N_8

4. CONCLUSION

In this study, the catalytic activity of transition-metal-doped double nanorings was investigated computationally for the nitrogen reduction reaction (NRR) using density functional theory (DFT). Multiple configurations and orientations of TM@double-nanoring complexes were modeled and optimized. The results revealed that only a few configurations exhibit structural stability. These stable geometries were further analyzed, and the most energetically favorable structures were selected for detailed investigation. The findings demonstrate that the selected metal–nanoring systems possess promising catalytic behavior toward NRR. Global reactivity parameters—including electrophilicity, chemical hardness, and softness provided valuable insight into the electronic characteristics of the systems and their suitability for nitrogen activation. The NRR mechanism was explored via the distal pathway using Ru@B_8N_8 as the catalytic center. This system offers a stable and confined environment for N_2 adsorption and activation, enabling efficient reaction progression. All NRR intermediates were optimized using a mixed basis-set approach, ensuring accurate description of the Ru active site while maintaining computational efficiency for the B_8N_8 nanocage. Frontier molecular orbital (FMO) and density of states (DOS) analyses revealed the key orbital interactions, charge-transfer processes, and electronic redistributions occurring during the reduction sequence. Natural bond orbital (NBO) analysis further clarified electron delocalization and bonding characteristics, confirming the electronic stability of the Ru@B_8N_8 catalyst. Additionally, the calculated HOMO–LUMO gaps and interaction energies provided insights into the reactivity, adsorption strength, and stabilization of NRR intermediates along the distal pathway.

Overall, the combined structural, energetic, and electronic evaluations highlight Ru@B_8N_8 as an efficient, stable, and highly promising single-atom catalyst for ammonia synthesis. The integrated analysis of HOMO–LUMO gaps, DOS spectra, NBO charge transfer, and mechanistic behavior offers a comprehensive understanding of its catalytic performance. This work identifies Ru@B_8N_8 as a strong candidate for sustainable and efficient nitrogen reduction catalysis.

REFERENCES

1. Tang, X., *et al., Computational screening of single-atom catalysts supported on Al12N12 nanocage for nitrogen reduction reaction.* Materials Today Communications, 2024. 4 0: p. 109509.
2. Pai, S.J., C.L. Heald, and J.G. Murphy, *Exploring the global importance of atmospheric ammonia oxidation.* ACS Earth and Space Chemistry, 2021. 5(7): p. 1674-1685.
3. Palys, M.J., *et al., Renewable ammonia for sustainable energy and agriculture: vision and systems engineering opportunities.* Current opinion in chemical engineering, 2021. 31: p. 100667.
4. Lim, J., *et al., Ammonia and nitric acid demand for fertilizer use in 2050.* ACS Energy Letters, 2021. 6(10): p. 3676-3685.
5. Zhou, D., *et al., Sustainable ammonia production by non-thermal plasmas: Status, mechanisms, and opportunities.* Chemical Engineering Journal, 2021. 421: p. 129544.
6. Hasan, M.H., *et al., A comprehensive review on the recent development of ammonia as a renewable energy carrier.* Energies, 2021. 14(13): p. 3732.
7. Bicer, Y., *et al., Impact assessment and environmental evaluation of various ammonia production processes.* Environmental management, 2017. 59: p. 842855.
8. Erisman, J.W., *et al., How a century of ammonia synthesis changed the world.* 2008. 1(10): p. 636-639.
9. Liu, H., *Ammonia synthesis catalysts: innovation and practice*. 2013: World Scientific.

10. Lan, R., J.T. Irvine, and S.J.I.j.o.h.e. Tao, *Ammonia and related chemicals as potential indirect hydrogen storage materials.* 2012. 37(2): p. 1482-1494.
11. MacFarlane, D.R., *et al., A roadmap to the ammonia economy.* 2020. 4(6): p. 1186-1205.
12. Soumare, A., *et al., Exploiting biological nitrogen fixation: a route towards a sustainable agriculture.* Plants, 2020. 9(8): p. 1011.
13. Davies-Barnard, T. and P. Friedlingstein, *The global distribution of biological nitrogen fixation in terrestrial natural ecosystems.* Global Biogeochemical Cycles, 2020. 34(3): p. e2019GB006387.
14. Wen, A., *et al., Enabling biological nitrogen fixation for cereal crops in fertilized fields.* ACS synthetic biology, 2021. 10(12): p. 3264-3277.
15. Mus, F., *et al., Exploring the alternatives of biological nitrogen fixation.* Metallomics, 2018. 10(4): p. 523-538.
16. Zhao, X., *et al., Comprehensive understanding of the thriving ambient electrochemical nitrogen reduction reaction.* Advanced Materials, 2021. 33(33): p. 2007650.
17. Wan, Y., J. Xu, and R. Lv, *Heterogeneous electrocatalysts design for nitrogen reduction reaction under ambient conditions.* Materials Today, 2019. 27: p. 6990.
18. Lv, X., L. Kou, and T. Frauenheim, *Hydroxyl-boosted nitrogen reduction reaction: the essential role of surface hydrogen in functionalized MXenes.* ACS applied materials & interfaces, 2021. 13(12): p. 14283-14290.
19. Hu, X., X. Li, and N.Q. Su, *Exploring Nitrogen Reduction Reaction Mechanisms with Graphyne-Confined Single-Atom Catalysts: A Computational Study Incorporating Electrode Potential and pH.* The Journal of Physical Chemistry Letters, 2024. 15(38): p. 9692-9705.
20. Mebs, S. and J. Beckmann, *In silico activation of dinitrogen with a light atom molecule.* Physical Chemistry Chemical Physics, 2022. 24(35): p. 20953-20967.
21. Laplaza, C.E. and C.C. Cummins, *Dinitrogen cleavage by a three-coordinate molybdenum (III) complex.* Science, 1995. 268(5212): p. 861-863.
22. McWilliams, S.F. and P.L. Holland, *Dinitrogen binding and cleavage by multinuclear iron complexes.* Accounts of chemical research, 2015. 48(7): p. 2059-2065.
23. Jiang, L., *et al., New mechanistic insights into electrokinetic competition between nitrogen reduction and hydrogen evolution reactions.* Advanced Energy Materials, 2024. 14(28): p. 2303809.
24. Liu, J.J.A.C., *Catalysis by supported single metal atoms.* 2017. 7(1): p. 34-59.
25. Zhang, H., S. Fang, and Y.H.J.C.R. Hu, *Recent advances in single-atom catalysts for CO oxidation.* 2022. 64(3): p. 491-532.
26. Yang, X.-F., *et al., Single-atom catalysts: a new frontier in heterogeneous catalysis.* 2013. 46(8): p. 1740-1748.
27. Yang, B., *et al., Recent progress in electrochemical synthesis of ammonia from nitrogen: strategies to improve the catalytic activity and selectivity.* 2021. 14(2): p. 672-687.
28. Liao, G., *et al., Review of carbon-based catalysts for electrochemical nitrate reduction and green ammonia synthesis.* 2024. 26(24): p. 11797-11831.
29. Montoya, J.H., *et al., The challenge of electrochemical ammonia synthesis: a new perspective on the role of nitrogen scaling relations.* 2015. 8(13): p. 21802186.
30. Zhang, Y., *et al., Mo2C embedded on nitrogen-doped carbon toward electrocatalytic nitrogen reduction to ammonia under ambient conditions.* 2021. 46(24): p. 13011-13019.
31. Xiao, S., *et al., Boron and nitrogen dual-doped carbon nanospheres for efficient electrochemical reduction of N 2 to NH 3.* 2020. 56(3): p. 446-449.
32. Yang, C., *et al., High-Performance Field-Effect Sensing of Ammonia Based on High-Density and Ultrathin Silicon Nanowire Channels.* 2024. 9(11): p. 62846291.
33. Zhang, H., *et al., Single-atom catalysts: emerging multifunctional materials in heterogeneous catalysis.* 2018. 8(1): p. 1701343.
34. Skrabalak, S.E., *et al., Gold nanocages: synthesis, properties, and applications.* Accounts of chemical research, 2008. 41(12): p. 1587-1595.
35. Furukawa, H., *et al., The chemistry and applications of metal-organic frameworks.* Science, 2013. 341(6149): p. 1230444.
36. Zhou, H.-C., J.R. Long, and O.M. Yaghi, *Introduction to metal–organic frameworks*. 2012, ACS Publications. p. 673-674.
37. Cote, A.P., *et al., Porous, crystalline, covalent organic frameworks.* science, 2005. 310(5751): p. 1166-1170.
38. Hasell, T. and A.I. Cooper, *Porous organic cages: soluble, modular and molecular pores.* Nature Reviews Materials, 2016. 1(9): p. 1-14.
39. Wang, A., J. Li, and T. Zhang, *Heterogeneous single-atom catalysis.* Nature Reviews Chemistry, 2018. 2(6): p. 65-81.
40. Qiao, B., *et al., Single-atom catalysis of CO oxidation using Pt1/FeO x.* Nature chemistry, 2011. 3(8): p. 634-641.
41. Wang, C., *et al., d- and p-Block single-atom catalysts supported by BN nanocages toward electrochemical reactions of N2 and O2.* Physical Chemistry Chemical Physics, 2023. 25(37): p. 25761-25771.
42. Yang, X., *et al., Metal-Encapsulated Boron Nitride Nanocages for Solar-Driven Nitrogen Fixation.* The Journal of Physical Chemistry C, 2020. 124(43): p. 23798-23806.
43. Allangawi, A., *et al., Decorating Mg12O12 Nanocage with Late First-Row Transition Metals To*

Act as Single-Atom Catalysts for the Hydrogen Evolution Reaction. ACS Omega, 2023. 8(41): p. 37820-37829.
44. Shen, X. and Q. Zhang, *Rational Design of Novel Single-Atom Catalysts of Transition-Metal-Doped 2D AlN Monolayer as Highly Effective Electrocatalysts for Nitrogen Reduction Reaction.* Molecules, 2024. 29(23): p. 5768.
45. Gnanasekar, P., *et al.*, *Protecting and Enhancing the Photoelectrocatalytic Performance of InGaN Nanowires toward Nitrogen Reduction to Ammonia Synthesis.* ACS Applied Energy Materials, 2023. 6(21): p. 10784-10793.
46. Shivaleela, B. and S. Hanagodimath. *UV-Visible Spectra, HOMO-LUMO Studies on Coumarin Derivative Using Gaussian Software*. in *Conference Proceedings of one day online International Conference on Advanced Materials*. 2020.
47. Tsipis, A.C., *RETRACTED: DFT flavor of coordination chemistry.* Coordination Chemistry Reviews, 2014. 272: p. 1-29.
48. Juanes, M., *et al.*, *Hydrogen Bonding in the Dimer and Monohydrate of 2-Adamantanol: A Test Case for Dispersion-Corrected Density Functional Method* Molecules, 2022. 27(8): p. 2584.
49. Khan W, Ullah S, Ullah S, Asghar R, Khan M, Zafar L, ur Rehman S. Quantitative Determination of Fluoride in Aqueous Samples Using the Spectroquant Photometric Fluoride Test. Sch Int J Chem Mater Sci. 2025;8(5):279-89.
50. Ahmad U, Khan AM, Ali A, Zeeshan A, Khanim A, Nazir S, Imran SH, Ibrahim A, Raza A. Designing Nanoparticle-Driven Materials for High-Performance Applications a Multidisciplinary Review. Sch Acad J Biosci. 2025 Jan; 1:148-58.
51. Khan M, Asghar R, ur Rehman S, Raza K, Anwar S. Sensor Application of Co-Polymer of Pyrrole and Aniline for Volatile Organic Compounds: A DFT Study. The Metascience. 2025 Feb 24;3(1):1-20.
52. Khan, M., Abdur Rab, M.M., Ullah, S., Sadiq Ur Rehman, R.A. and Zafar, L., 2025. Density Functional Theory (DFT) Investigation of Thiophene-Pyrrole Copolymers for VOC and Inorganic Gas Sensing Applications. *Sch Int J Chem Mater Sci*, *8*(5), pp.237-249.